Available online at www.sciencedirect.com
ScienceDirect
Journal of Sound and Vibration 313 (2008) 113–133
JOURNAL OF SOUND AND VIBRATION
www.elsevier.com/locate/jsvi

Predicting tonal noise from a high rotational speed centrifugal fan

S. Khelladi*, S. Kouidri, F. Bakir, R. Rey

Ecole Nationale Supérieure d'Arts et Métiers, LEMFi-ENSAM, 151, Boulevard de l'Hospital, Paris 75013, France

Received 24 October 2006; received in revised form 16 November 2007; accepted 19 November 2007
Available online 2 January 2008

Abstract

Prediction of noise generated by centrifugal fans is much more complex than prediction noise generated by axial fans. A complete, aerodynamic and aeroacoustic, investigation of the tonal noise of a high rotational speed centrifugal fan is proposed in this paper. The studied fan is made up of an impeller, a diffuser and a return channel. The purpose of this work is to understand the nature of noise generated within this type of machine. An aeroacoustic model based on the Ffowcs Williams and Hawkings equation is used to predict dipole and monopole tonal noises in the frequency domain. Showing the importance of the monopole source in this kind of fans constitutes the main contribution in these research tasks. A numerical simulation of the fluid flow validated by experiments, enables to obtain the fluctuating forces and normal velocity on the impeller and diffuser blades needed for the aeroacoustic computation.

1. Introduction

A widespread industrial application of centrifugal fans has been found on literature. As a type of turbomachinery, the centrifugal fans have been widely adopted by public facilities and electronic industries, due to their large capacity of mass flow and their compactness. A state-of-the-art review has shown the potential development in the field of centrifugal compressors [1]. It was pointed out that many machines having moderate efficiency and low aeroacoustic performances are still in operation and could certainly be improved by making use of today's technology.

Shrouded impellers are usually used in high-rotational speed centrifugal fans. The impellers are linked downstream by a vaned diffuser and a return channel, see Fig. 1, in practice the unit is covered by a casing.

The diffuser transforms a part of kinetic energy, available at the impeller exit, into static pressure rise. The return channel takes out the swirl while guiding the flow to the downstream duct. For such a kind of turbomachinery, the nature of the impeller–diffuser interaction and the generating acoustic noise are inherently becoming two major concerns of research. Nowadays, there is a great deal of studies concerning the effects of impeller–diffuser interaction on aerodynamics and aeroacoustics performances.

*Corresponding autor.
E-mail address: sofiane.khelladi@paris.ensam.fr (S. Khelladi).

0022-460X/$ - see front matter © 2007 Elsevier Ltd. All rights reserved.
doi:10.1016/j.jsv.2007.11.044

Nomenclature

c_0	velocity of sound in a medium at rest
D	Doppler amplification factor due to the moving source (in the relative reference frame)
f	a function taking into account the geometry and the kinematics of the moving surface when $f(\mathbf{x}, t) = 0$
$\mathbf{F}$	force due to interaction of the flow with the moving surface
F_i	force components ($i = x, y, z$)
H	Heaviside function
$\mathbf{M}$	Mach number associated to the absolute velocity of the source
M_r	Mach number of the sources in the direction of listening point given by $M_r = \frac{1}{r}\mathbf{r} \cdot \mathbf{M}$
p'	acoustic pressure
p_0	standard reference pressure
P_0	mean pressure on the impeller blade
$\mathbf{r}$	distance between the observer and the source given by $\mathbf{r} = \mathbf{x} - \mathbf{y}$
t	reception time
T_{ij}	Lighthill's tensor
V_n	velocity normal to the moving surface
V_{si}	velocity at the moving surface
$\mathbf{x}$	position of the observer
$\mathbf{y}$	position of the source
δ	Dirac function
δ_{ij}	Kronecker symbol
ρ'	fluctuating density
σ'_{ij}	constraint tensor given by $\sigma'_{ij} = \tau_{ij} - p\delta_{ij}$
τ	emission time
τ_{ij}	shear stress tensor

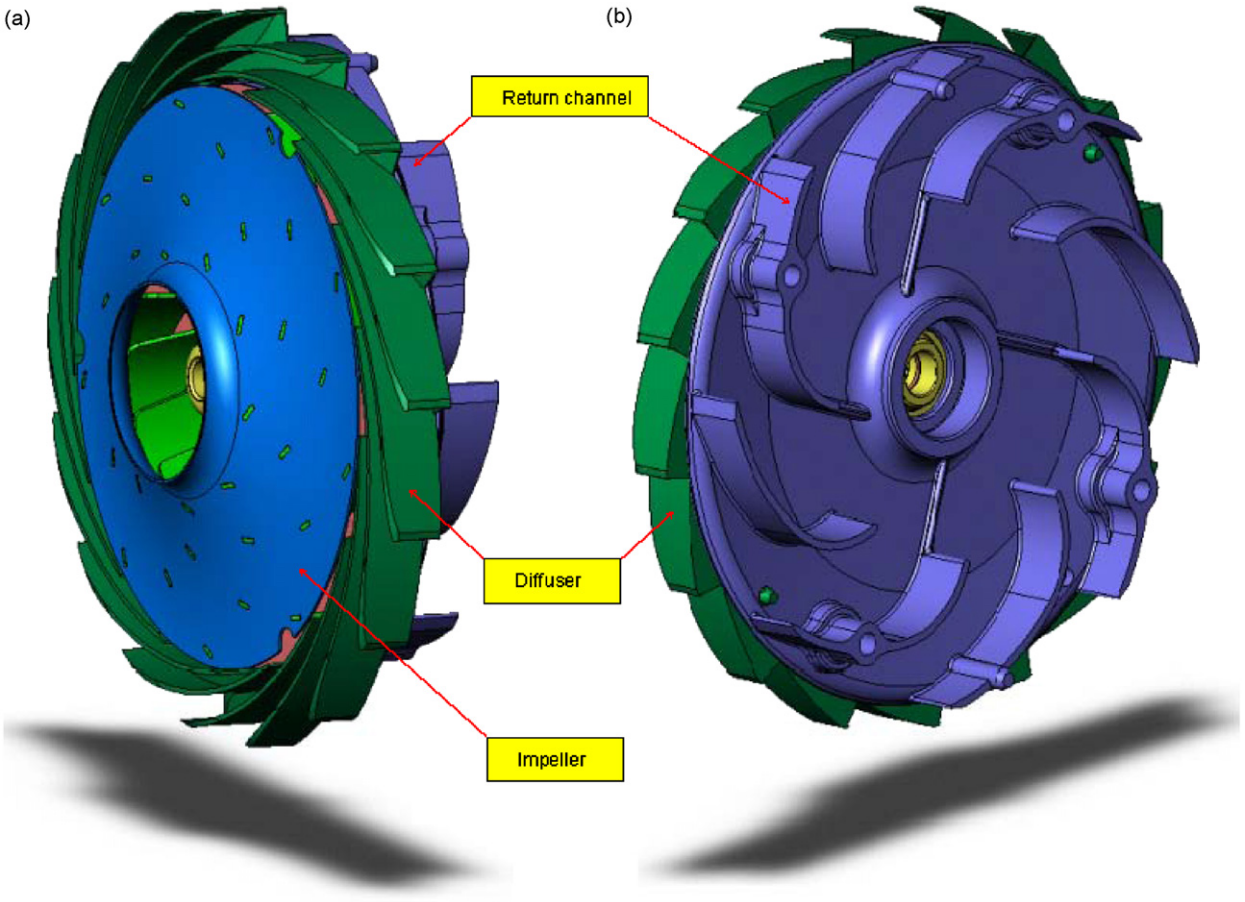

Fig. 1. Centrifugal fan: (a) upstream view: (b) downstream view.

The development of powerful numerical algorithms and robust commercial tools enables to deeply understand the unsteady flow field and the mechanisms of noise generation, therefore, the advanced CFD tools make the optimized design of centrifugal fan possible [2–4]. The three-dimensional unsteady viscous flow solution was numerically obtained by means of powerful computational facilities and robust software together with very consumptive calculation time [5].

It is well known, despite the knowledge accumulated over the past few decades on the mechanisms of noise generation on air delivery systems, that the prediction of such a flow field and the resulting acoustic pressure, by numerical means, is still difficult. This is due to our inability to model the turbulent viscous flow with sufficient accuracy and the complicated nature of flow through such machines [6].

Many experimental and theoretical studies contributed to a better understanding of the noise generated by fans. Neise presents in Refs. [7–9] a large review of noise reduction in centrifugal fans, the investigations were based on measurement techniques and results. The same work has been done by Parrondo-Gayo et al. [10] concerning noise and pressure fluctuations prediction in pumps. In Ref. [11] Jeon et al. used a 2D vortex method for a non-viscous fluid coupled to the far-field Ffowcs Williams and Hawkings model to predict the dipole tonal noise of a centrifugal fan in a vacuum cleaner. The viscous and compressibility effects are not taken into account. Maaloum et al. presents in Ref. [12] a modeling of the tonal noise generated by an axial fan. A RANS model coupled to the far-field Ffowcs Williams and Hawkings model is used. Only the dipole term is taken into account.

The centrifugal fan noise is usually dominated by tones produced by the impeller blade passage. The resulted tonal noise corresponds to the blade passage frequency (BPF) and its higher harmonics. This is a consequence of the strong interaction between the impeller and the diffuser blades at their interface.

In this paper, a vacuum cleaner motor-fan was used. The aerodynamic and geometrical characteristics at its operating point are given, respectively, in Tables 1 and 2.

A methodology based on a hybrid modeling of the aeroacoustic behavior of a high-rotational speed centrifugal fan is presented in this paper. The main objective is to predict noise generated by this machine and to take into account the effect of monopole and dipole sources on the overall noise. Ffowcs Williams and Hawkings model is used to predict the far-field tonal noise radiated by the centrifugal fan. The fluctuating forces and normal velocity are obtained by an aerodynamic study of the centrifugal fan [13,5].

Table 1
Aerodynamic characteristics at operating point

Description	Value
Head (H)	1300 (m)
Flow rate (Q)	35×10^{-3} (m^3s^{-1})
Rotational speed (N)	34 560 (rev/min)
Specific speed ($N_{sq} = \frac{N\sqrt{Q}}{H^{3/4}}$)	29

Table 2
Geometrical characteristics of the centrifugal fan

Description	Impeller	Diffuser	Return channel
Radius of blade inlet (mm)	18	52.7	60
Span of the blade at the entry (mm)	13	6.48	11
Inlet blade angle (deg.)	64	85	74
Inclination Angle of the blade inlet (deg.)	85.8	0	0
Radius of blade exit (mm)	52	66.1	33
Span of the blade at the exit (mm)	5.4	8.43	12
Angle of blade exit (deg.)	64	71.6	15
Inclination angle of the blade exit (deg.)	0	0	0
Blade number	9	17	8
Blade thickness (mm)	0.8	0.9	1.6

2. Aeroacoustic analogy

The Ffowcs Williams and Hawkings (FW&H) equation is an exact rearrangement of the continuity and the momentum [14,15] into the form of an inhomogeneous wave equation (1). This equation has two surface source terms, known as thickness and loading sources, and a volume source term, known as the quadruple source derived from the original Lighthill [16,17] theory. FW&H equation is given by

$$\frac{\partial^2\rho'}{\partial t^2}-c_0^2\frac{\partial^2\rho'}{\partial x_i^2}=\frac{\partial^2}{\partial x_i\partial x_j}\left(T_{ij}H(f)\right)+\frac{\partial}{\partial x_i}\left(\sigma'_{ij}\delta(f)\frac{\partial f}{\partial x_j}\right)+\frac{\partial}{\partial t}\left(\rho_0 V_{si}\delta(f)\frac{\partial f}{\partial x_i}\right) \tag{1}$$

FW&H equation is used when the flow interacts with a rotating surface which is equivalent to an acoustic medium at rest forced by 3 source distributions [18].

Source terms of Eq. (1) are defined as follows:

(1) quadrupole source $\partial^2/\partial x_i\partial x_j(T_{ij}H(f))$: is a volume distribution due to the flow outside the surfaces.
(2) Dipole source or loading source $\partial/\partial x_i(\sigma'_{ij}\delta(f)\partial f/\partial x_j)$: is a surface distribution due to the interaction of the flow with the moving bodies [19].
(3) Monopole source or thickness source $\partial/\partial t(\rho_0 V_{si}\delta(f)\partial f\partial x_i)$: is a surface distribution due to the volume displacement of fluid during the motion of surfaces.

Although the quadrupole source contribution is insignificant in many subsonic applications, substantially more computational resources are needed for volume integration when the quadrupole source is required.

2.1. FW&H equation solution

The noise is radiated in free field. Reflexions, diffractions, scattering as well as the casing effect are not taken into account. Fig. 2 presents a measurement of the attenuation factor of the casing versus frequency. The test bench consists on a mono-frequency source and a microphone placed at 5 mm at each sides of the casing. The figure shows that the attenuation of the casing is about 1.4 dB around the BPF. It shows also that the attenuation is increasing at high frequencies. So the assumption of free field is a good approximation at BPF.

Using a free field Green's function form and the far-field assumption to solve Eq. (1), the solution of the FW&H equation in a moving reference frame related to the surface is given by

$$\begin{aligned}c_0^2\rho'(\mathbf{x},t)=&\frac{1}{4\pi}\int\int\int_V\frac{r_i r_j}{r^3Dc_0^2}\frac{\partial}{\partial\tau}\left[\frac{1}{D}\frac{\partial}{\partial\tau}\left(\frac{T_{ij}}{D}\right)\right]\mathrm{d}V\\&-\frac{1}{4\pi}\int\int_S\frac{r_i}{c_0Dr^2}\frac{\partial}{\partial\tau}\left(\frac{F_i}{D}\right)\mathrm{d}S-\frac{1}{4\pi}\int\int_S\frac{\partial}{\partial t}\left(\frac{\rho_0V_n}{rD}\right)\mathrm{d}S,\end{aligned} \tag{2}$$

with $\tau=t-r/c_0$ and $D=|1-M_r|$.

In far field, $c_0^2\rho'$ can be assimilated to an acoustic pressure p', the expansion is assumed isentropic [15].

In order to calculate the acoustic pressure due to the blade passage tonal noise produced by centrifugal fans Eq. (2) is written in frequency domain. Let us consider a centrifugal impeller turning at a velocity Ω. The angular position of a point on the blade is related to the moment of noise emission τ by $\Psi=\Omega\tau+\Psi_0$ where Ψ_0 is the initial position at $\tau=0$. Suppose that $\Psi_0=0$ at $\tau=0$.

The Fourier transform allows the passage from temporal to frequential domain. It is given by

$$\Phi^{(s)}(\mathbf{x})=\frac{\Omega}{2\pi}\int_0^{2\pi/\Omega}\Phi(\mathbf{x},t)\mathrm{e}^{\mathrm{i}s\Omega t}\,\mathrm{d}t, \tag{3}$$

with $\Phi=p',T_{ij},\mathbf{F}$ or V_n.

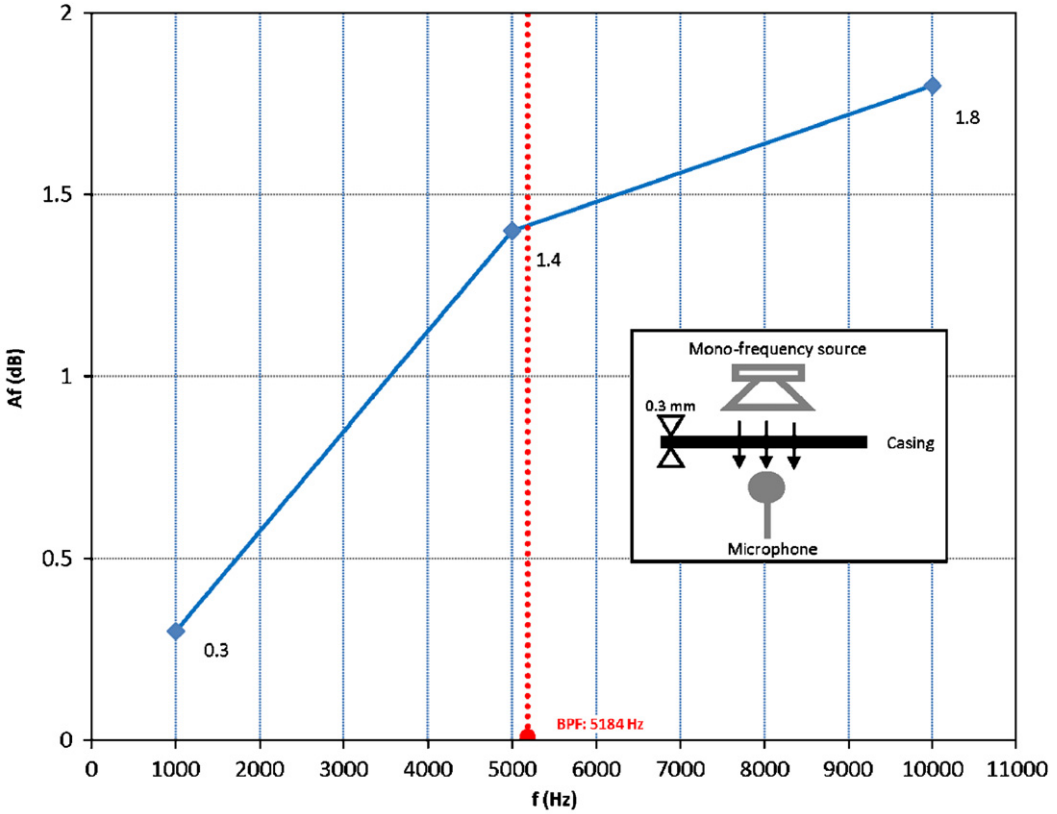

Fig. 2. Attenuation factor vs. frequency.

The acoustic pressure due to the interferences between the various rotating elements (impeller blades) is given by

$$p'^{(s)}(\mathbf{x}) = \sum_{j=1}^{\mathrm{ns}} p_j'^{(s)}(\mathbf{x}), \tag{4}$$

ns is the number of sources.

Eq. (4) can also be the sum of sources of several types (dipole and monopole) fixed or mobile (rotor and stator).

As the flow field is subsonic, the quadrupole noise is neglected.

Fourier transform and integration by parts of the acoustic pressure of both dipole and monopole terms of Eq. (2) give:

- *Dipole source*:

$$p'^{(s)}_{\mathrm{load}}(\mathbf{x}) = \frac{\mathrm{i}s\Omega^2}{8\pi^2 c_0} \int\int_S \int_0^{2\pi/\Omega} \frac{\mathbf{r}\cdot\mathbf{F}}{r^2} \mathrm{e}^{\mathrm{i}st\Omega(\tau+(r/c_0))}\,\mathrm{d}\tau\,\mathrm{d}S. \tag{5}$$

- *Monopole source*:

$$p'^{(s)}_{\mathrm{thickness}}(\mathbf{x}) = \frac{\mathrm{i}s\Omega^2\rho_0}{8\pi^2 r_o} \int\int_S \int_0^{2\pi/\Omega} V_n \mathrm{e}^{\mathrm{i}s\Omega(\tau+(r/c_0))}\,\mathrm{d}\tau\,\mathrm{d}S. \tag{6}$$

2.2. FW&H equation solution for a centrifugal fan (moving source)

In Fig. 3, S is a noise source rotating around e_3 with an angular velocity Ω and a distance r_s. $\mathbf{F}$, a force applied by the fluid on the surface on S, it is defined by its radial, tangential and axial components (F_r, F_t, F_a). O is an observer defined by (r_o, φ, θ) and $\mathbf{r}$ the distance between S and O.

According to Fig. 1, the distance between the source and the observer is given by

$$\mathbf{r} = \begin{pmatrix} r_o \sin(\theta)\cos(\varphi) - r_s \cos(\Omega\tau) \\ r_o \sin(\theta)\sin(\varphi) - r_s \sin(\Omega\tau) \\ r_o \cos(\theta) \end{pmatrix}. \tag{7}$$

In far field, $r_o \gg r_s$, so r is given by

$$r \cong r_o - r_s \sin(\theta)\cos(\Omega\tau - \varphi). \tag{8}$$

Over each element dS of the impeller surface a force $\mathbf{F}$ is applied, it is defined by

$$\mathbf{F} = \begin{pmatrix} F_r \cos(\Omega\tau) + F_t \sin(\Omega\tau) \\ F_r \sin(\Omega\tau) - F_t \cos(\Omega\tau) \\ F_a \end{pmatrix} = \begin{pmatrix} F_1 \\ F_2 \\ F_3 \end{pmatrix}. \tag{9}$$

The direction of $\mathbf{F}$ components depends on several parameters: the direction of the source rotation, the fluid flow direction and the source position.

Replacing $\mathbf{F}$ and $\mathbf{r}$ by their value in Eqs. (5) and (6), and using Jacobi-Anger Expansion expressed by

$$e^{-iz\cos(\psi)} = \sum_{q=-\infty}^{\infty} (-i)^q J_q(z) e^{-iq\psi},$$

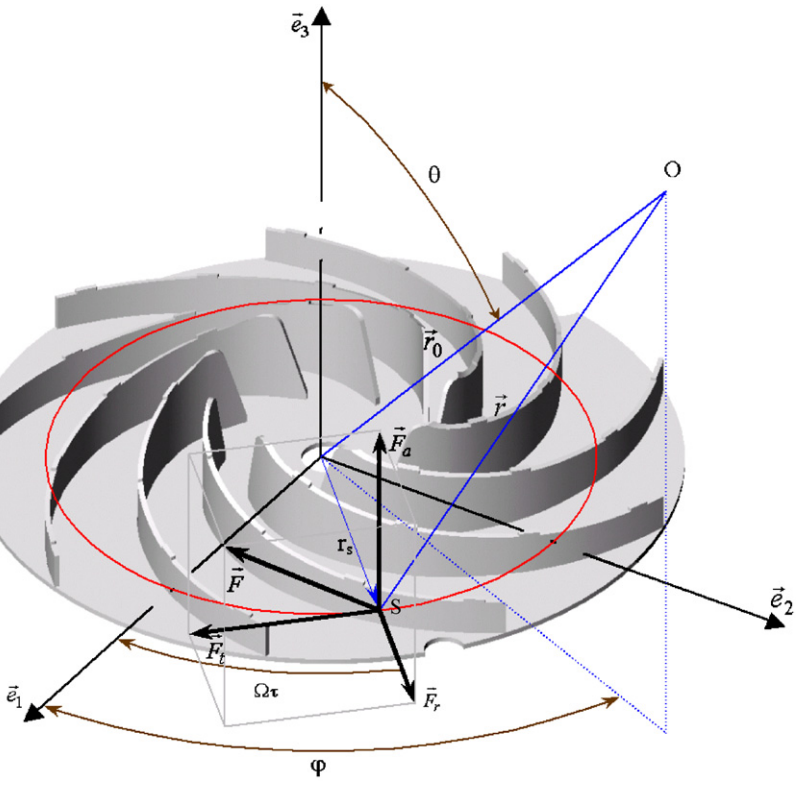

Fig. 3. Reference of the impeller.

the acoustic pressure at the mth harmonic produced by a centrifugal impeller of Z equivalent and equidistant blades is given by

- *Dipole source*:

$$p'^{(m)}_{\text{load}}(\mathbf{x}) = \frac{\mathrm{i}mZ^2\Omega}{4\pi c_0 r_o} \mathrm{e}^{\mathrm{i}mZ(r_o/c_0)\Omega} \int\int_S \sum_{k=-\infty}^{+\infty} \mathrm{e}^{\mathrm{i}(mZ-k)(\varphi-\pi/2)} \times \left\{ \mathrm{i}\sin(\theta) J'_{mZ-k}(A) F_r^{(k)} + \left[\cos(\theta) F_a^{(k)} - \frac{mZ-k}{mZM_{rs}} F_t^{(k)} \right] J_{mZ-k}(A) \right\} \mathrm{d}S. \tag{10}$$

- *Monopole source*:

$$p'^{(m)}_{\text{thickness}}(\mathbf{x}) = \frac{\mathrm{i}mZ^2\Omega\rho_0}{4\pi r_o} \mathrm{e}^{\mathrm{i}mZ\Omega(r_o/c_0)} \times \int\int_S \sum_{k=-\infty}^{+\infty} \mathrm{e}^{\mathrm{i}(mZ-k)(\varphi-\pi/2)} J_{mZ-k}(A) V_n^{(k)} \, \mathrm{d}S, \tag{11}$$

where $A = mZ\Omega(r_s/c_0)\sin(\theta)$ and $M_{rs} = r_s\Omega/c_0$; $J_{mZ-k}(A)$: first kind Bessel function; and $J'_{mZ-k}(A) = \frac{1}{2}(J_{mZ-k-1}(A) - J_{mZ-k+1}(A))$.

A near-identical formulation of Eqs. (10) and (11) is presented by Goldstein in Ref. [15].

2.3. FW&H equation solution for a diffuser

Eq. (5) is also used to calculate the acoustic pressure radiated by a source on a diffuser blade. **F** and **r** are expressed in the absolute reference frame knowing that the elementary sources on the surface are fixed. The sign of the force components **F** is a function of the flow and the fixed surface directions. According to Fig. 4, the expression of **r** and **F** becomes:

$$\mathbf{r} = \begin{pmatrix} r_o \sin(\theta)\cos(\varphi) - r_s\cos(\alpha) \\ r_o \sin(\theta)\sin(\varphi) - r_s\sin(\alpha) \\ r_o\cos(\theta) \end{pmatrix}, \tag{12}$$

$$\mathbf{F} = \begin{pmatrix} F_r\cos(\alpha) + F_t\sin(\alpha) \\ F_r\sin(\alpha) - F_t\cos(\alpha) \\ F_a \end{pmatrix}. \tag{13}$$

In far field r is given by

$$r \cong r_o - r_s\sin(\theta)\cos(\alpha - \varphi), \tag{14}$$

α is the angular position of the diffuser blade in the absolute reference frame. All the geometric parameters (radius, angles,...) are identical to the case of the rotating source.

The diffuser is generally placed downstream the impeller, it is used for recovering a part of the pressure energy lost by the impeller in rotation. The tonal noise radiated by the diffuser is produced at the harmonics of the BPF of the impeller.

Replacing **F** and **r** by their value, the acoustic pressure produced by a diffuser of V blades is given by:

$$p'^{(m)}_{\text{load}}(\mathbf{x}) = \frac{\mathrm{i}mZ\Omega}{4\pi c_0 r_o} \mathrm{e}^{\mathrm{i}mZ(r_o/c_0)\Omega} \int\int_S \sum_{j=0}^{V-1} \{ [\cos(\alpha_j - \varphi)\sin(\theta) F_r^{(m)} + \sin(\theta)\sin(\alpha_j - \varphi) F_t^{(m)} + \cos(\theta) F_a^{(m)}] \mathrm{e}^{\mathrm{i}mZ(\alpha_j - A\cos(\alpha_j - \varphi))} \} \, \mathrm{d}S, \tag{15}$$

with, $A = mZ\Omega(r_s/c_0)\sin(\theta)$ and $M_{rs} = \Omega r_s/c_0$.

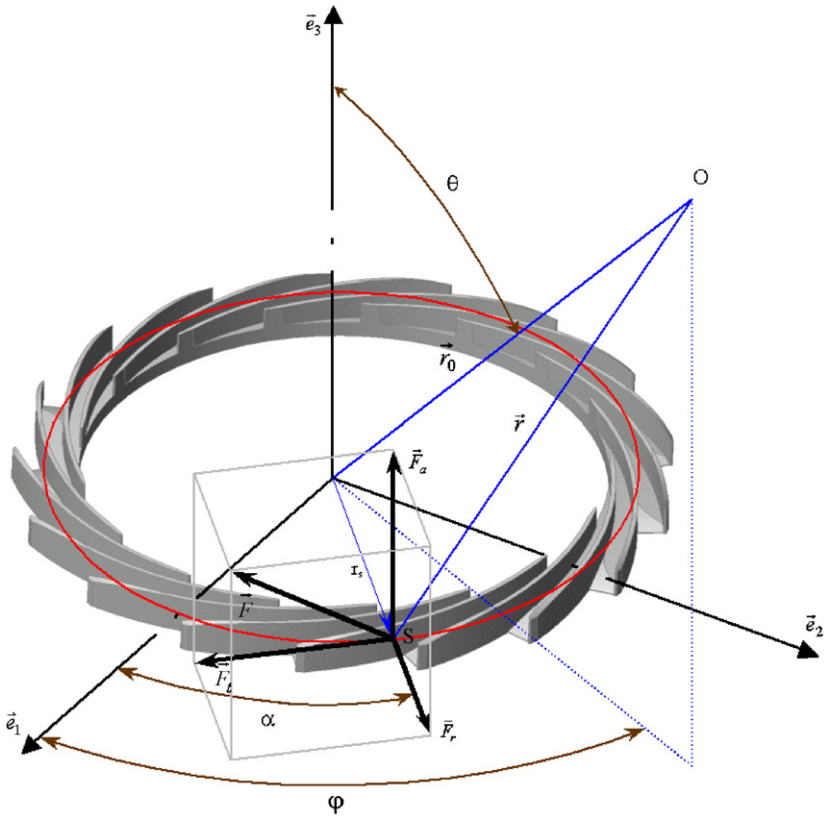

Fig. 4. Reference of the diffuser.

If the V blades are equivalent and equidistant then $\alpha_j = \mathrm{j}(2\pi/V) + \alpha_0$ where α_0 is the position of first blade of the diffuser defined as reference.

The harmonic rank of the acoustic pressure is the same as the one of the force components in Eq. (15), this implies that the observer receives a noise at the same frequency as that of the sources.

2.4. Compact sources

A source is compact if:

$$L \ll \frac{c_0 \bar{D}}{f_c}, \tag{16}$$

where L is a characteristic length of the source and f_c is the source frequency. $\bar{D}$ is the mean Doppler factor related to the overall source zone.

The numerical integration of Eqs. (10), (11) and (15) requires a surface discretization. The maximum size of the discretization for each element over the surface must satisfy the compactness condition (16).

Eqs. (10), (11) and (15) becomes:

Dipole source

- Impeller:

$$p'^{(m)}_{\mathrm{load1}}(\mathbf{x}) = \frac{imZ^2\Omega}{4\pi c_0 r_o} \mathrm{e}^{imZ(r_o/c_0)\Omega} \sum_{k=-\infty}^{+\infty} \mathrm{e}^{\mathrm{i}(mZ-k)(\varphi-\pi/2)} \times \left\{ \mathrm{i}\,\sin(\theta) J'_{mZ-k}(A) F_r^{(k)} + \left[\cos(\theta) F_a^{(k)} - \frac{mZ-k}{mZM_{rs}} F_t^{(k)} \right] J_{mZ-k}(A) \right\} S. \tag{17}$$

- Diffuser:

$$p'^{(m)}_{\text{load2}}(\mathbf{x}) = \frac{imZ\Omega}{4\pi c_0 r_o} e^{imZ(r_o/c_0)\Omega} \sum_{j=0}^{V-1} \{[\cos(\alpha_j - \varphi)\sin(\theta)F_r^{(m)} + \sin(\theta)\sin(\alpha_j - \varphi)F_t^{(m)} + \cos(\theta)F_a^{(m)}]e^{imZ(\alpha_j - A\cos(\alpha_j - \varphi))}\} S. \quad (18)$$

Monopole source

$$p'^{(m)}_{\text{thickness}}(\mathbf{x}) = \frac{imZ^2\Omega\rho_0}{4\pi r_o} e^{imZ\Omega(r_o/c_0)} \sum_{k=-\infty}^{+\infty} e^{i(mZ-k)(\varphi-\pi/2)} J_{mZ-k}(A) V_n^{(k)} S. \quad (19)$$

F and V_n are the equivalent force components exerted by the solid on the fluid and the equivalent normal velocity on the surface, respectively; $A = mZ\Omega(r_s/c_0)\sin(\theta)$ and $M_{rs} = (r_s\Omega/c_0)$.

The moving surfaces are divided into compact parts if they do not verify the compactness condition (16). Eqs. (17)–(19) are, then, applied for each compact part of the blade surface and the overall acoustic pressure is the sum of the acoustic pressure of each compact mesh.

A numerical simulation, validated by experimental tests, makes it possible to determine the temporal variation of the normal velocity and each component of the aerodynamic forces on the rotor and stator blades.

3. Aerodynamic study

The numerical simulations have been carried out with a finite volume code method using Fluent [20] to solve the full 3D Reynolds average Navier–Stokes equations.

3.1. Fluid volume modeling

For numerical stability reasons, two fluid volumes, one upstream and one downstream, are added. They do not simulate the actual geometry of the experimental equipment, they are added to the numerical model in order to reduce the effects of the inlet and outlet boundary conditions on the aerodynamic characteristics of the impeller inlet and the return channel outlet. This configuration results in the 3 non-conformal interfaces presented in Fig. 5.

3.2. Meshing

As the geometry of the fan is complex, a hybrid mesh is used: tetrahedral for the impeller and the diffuser–return channel volumes, hexahedral for upstream and downstream fluid volumes. A previous study of Khelladi et al. [5] shows that a grid of 4.4×10^6 meshes is considered to be sufficiently reliable to make the numerical modeling results independent to the mesh size.

3.3. Turbulence model

A statistical turbulence model was used within the framework of this numerical simulation. The $k-\omega$ SST (shear stress transport) model was adopted. It uses a treatment close to the wall combining a correction for high and low Reynolds number in order to predict separation on smooth surfaces [21].

3.4. Numerical model

The unsteady terms of conservation equations are implicit second-order discretized. A centered SIMPLE algorithm [22] is used for the pressure–velocity coupling and a second-order upwind discretization is used for the convection and diffusion terms. The conservation equations are solved using a segregated solver. The boundary conditions selected for this simulation are the velocity at the upstream volume inlet and the static

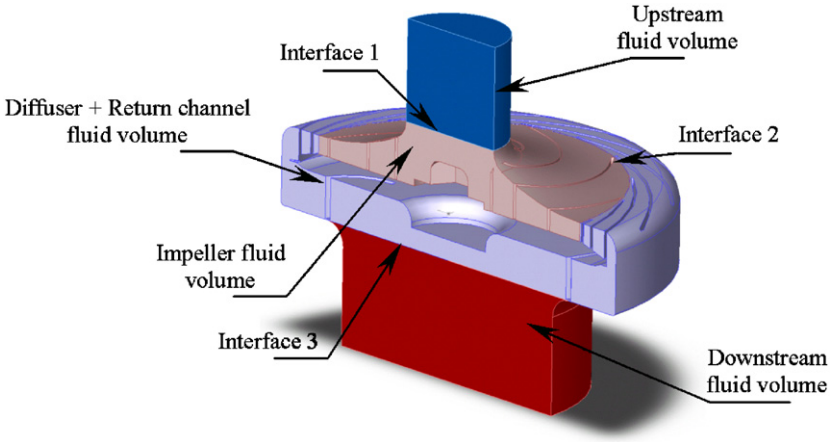

Fig. 5. Fluid volume cross section.

pressure at the downstream volume outlet. The value of the outlet pressure, applied as boundary condition at the exit part of the downstream volume, comes from the experimental measurement at the outlet side.

4. Application and results

4.1. Aerodynamics

Measurements were carried out on a test bench (see Fig. 6) equipped with an airtight box ($0.6 \times 0.6 \times 0.6\,m^3$), placed upstream the centrifugal fan. Kulite type dynamic sensors, with a diameter of 1.6 mm and a band-width of 125 kHz were used for the phase averaging pressure measurement. This allows the measurement of a static pressure up to 140 mbar and a fluctuating component up to 194 dBA. These aerodynamic data are transmitted to a digital oscilloscope (Gould Nicolet: Sigma 90) with 8 simultaneous channels whose band-width is 25 MHz and has a resolution of 12 bits.

The results obtained by numerical simulation are compared with the results of measurements. Fig. 8 presents the temporal evolution of the static pressure at five points of the impeller–diffuser interface, see Fig. 7, with an uncertainty of $\pm 2.5 \times 10^{-6}$ s on time and ± 2.5 mbar on the pressure.

At the impeller–diffuser interface, measurements were carried out by means of flush mounted Kulite sensors described in Fig. 6. In spite of their small dimensions and taking into account the narrow geometry of the area of measurement, they could not be laid out near the pressure and suction sides of the diffuser blades. The comparison of the results shows a rather good prediction of the pressure temporal signal. Fig. 8 demonstrates a strong interaction between the impeller and the diffuser blades.

Fig. 9 shows the instantaneous fluctuating pressure field on the pressure and the suction side of an impeller blade. The turbulent flow on the pressure side presents more significant fluctuations than those observed on the suction side. In addition, the areas close to the trailing edge are prone to a significant interaction with the leading edge of the diffuser. The acoustic noise is mainly generated by the interaction between the flow and the diffuser leading edges. So, the choice of this area as priority target of aeroacoustic optimization is consolidated.

The numerical simulation made it possible to calculate the unsteady forces and normal velocity on each element of the blades surface.

These two parameters will be used for the calculation of the noise radiated by the centrifugal fan.

Fig. 10 shows the variation of the force components applied to the blades over three time periods (three impeller rounds). The presence of 17 peaks corresponding to the 17 blades of the diffuser is noted over one time period. One also notices the significant contribution of the mean and fluctuating radial force on the overall force.

The axial component of the force is negligible compared to radial and tangential components.

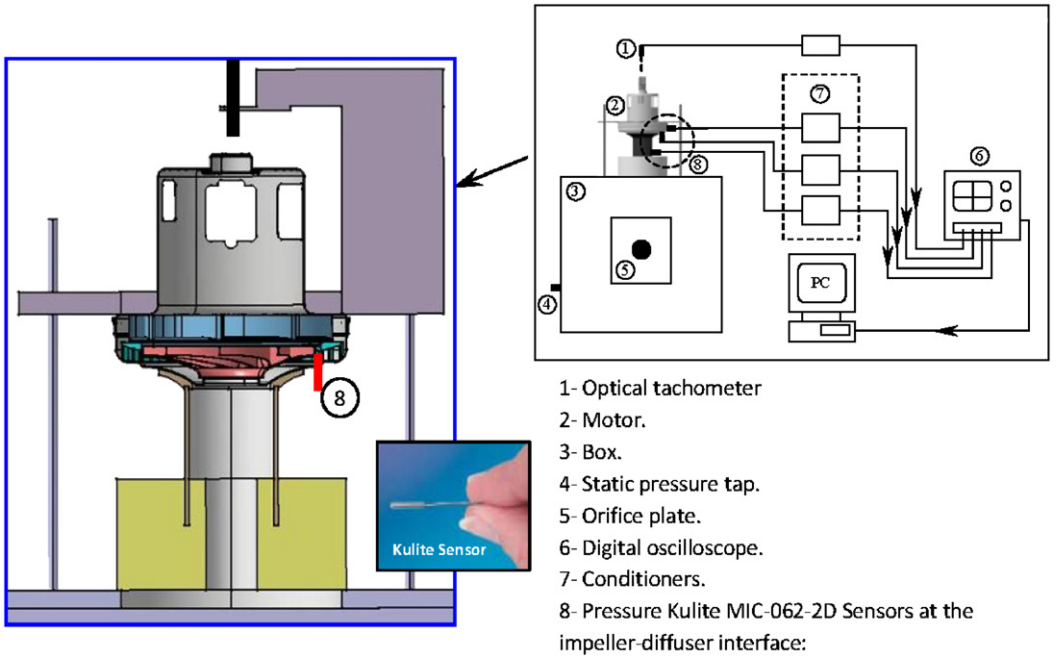

Fig. 6. Diagram of the test bench.

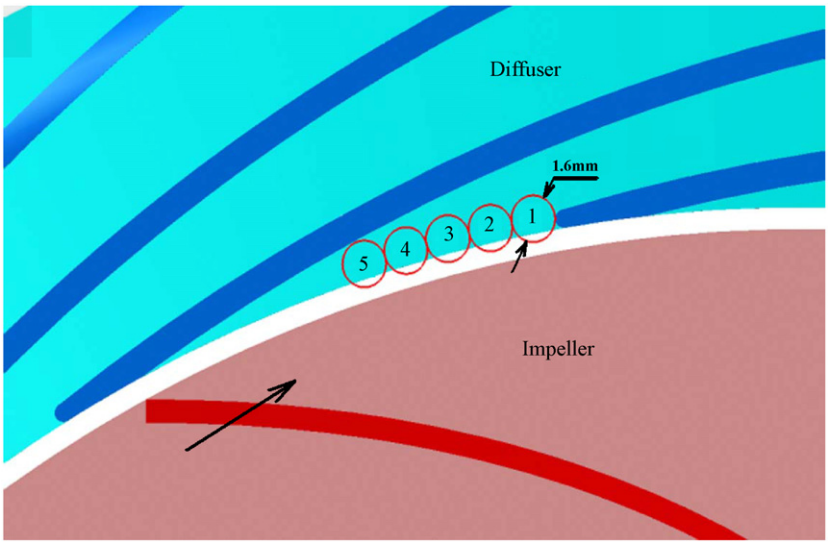

Fig. 7. Position of sensors on the impeller–diffuser interface.

The force fluctuation on a diffuser blade is presented in Fig. 11, the impeller blade passage is identified by 9 peaks during one period. The axial force is negligible in comparison with radial and tangential forces. These two components are negative as opposed to those acting on the impeller blades.

Fig. 12 shows the fluctuation of the normal velocity versus time. One finds the 17 peaks relating to the diffuser and the impeller blades interaction during one period. Normal velocity is a component of monopole

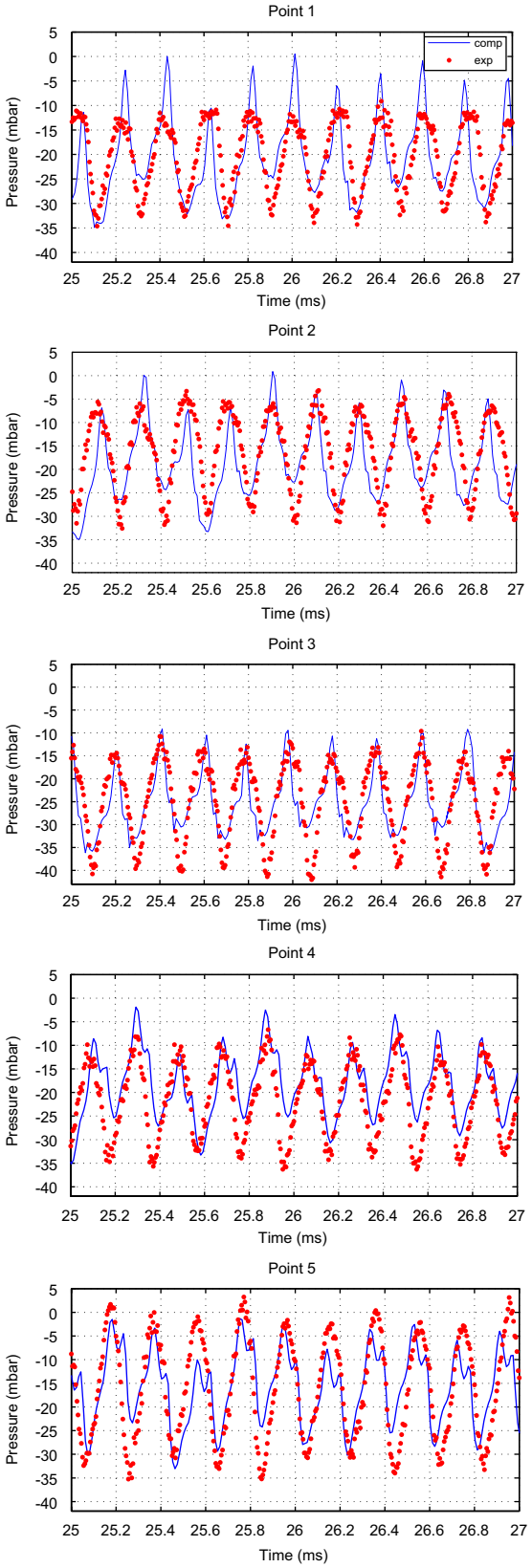

Fig. 8. Time history of the phase averaging static pressure on 5 azimuthal positions in the impeller–diffuser interface.

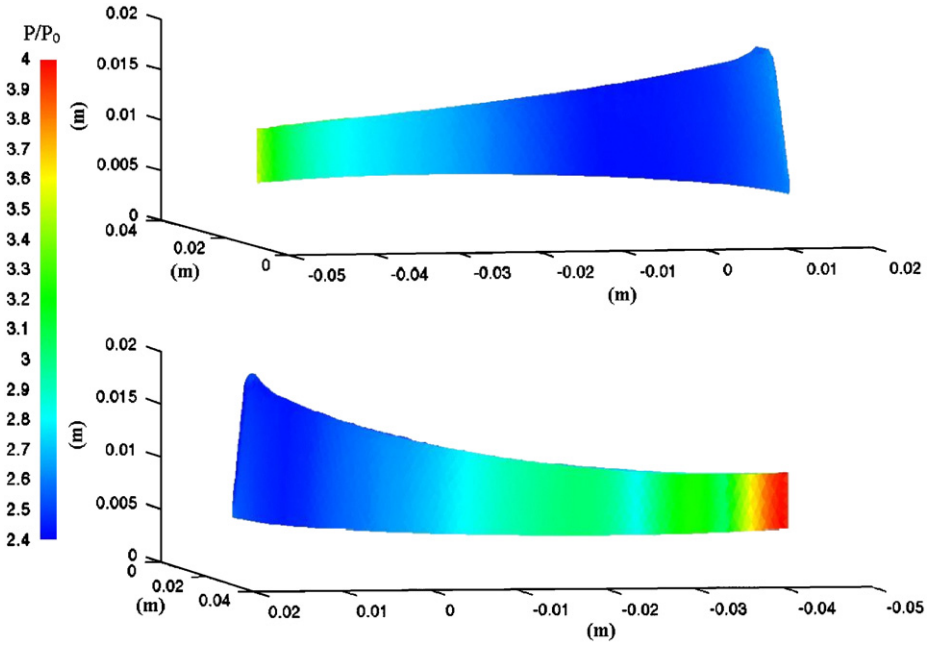

Fig. 9. Pressure field on an impeller blade: suction side (top), pressure side (bottom).

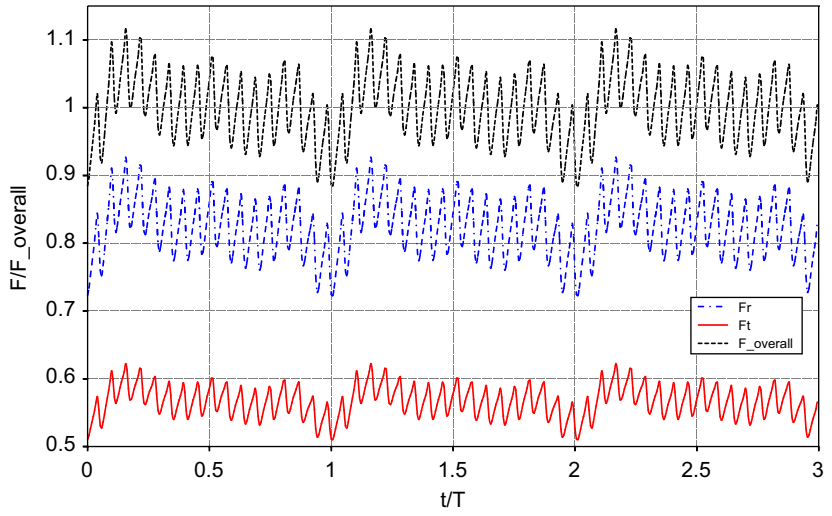

Fig. 10. Force fluctuation vs. time of radial, tangential and overall force over an impeller blade.

term in the FW&H equation, it is not negligible in the studied case. Its effect on the overall noise radiated by the centrifugal fan will be shown thereafter.

4.2. Aeroacoustics

In case of the absence of diffuser in numerical modeling, calculations will not make it possible to perceive the tonal noise due to the pressure fluctuation. Indeed, without the use of an upstream disturbance, the Reynolds average Navier–Stokes equations are not able to predict the pressure fluctuations in the case of

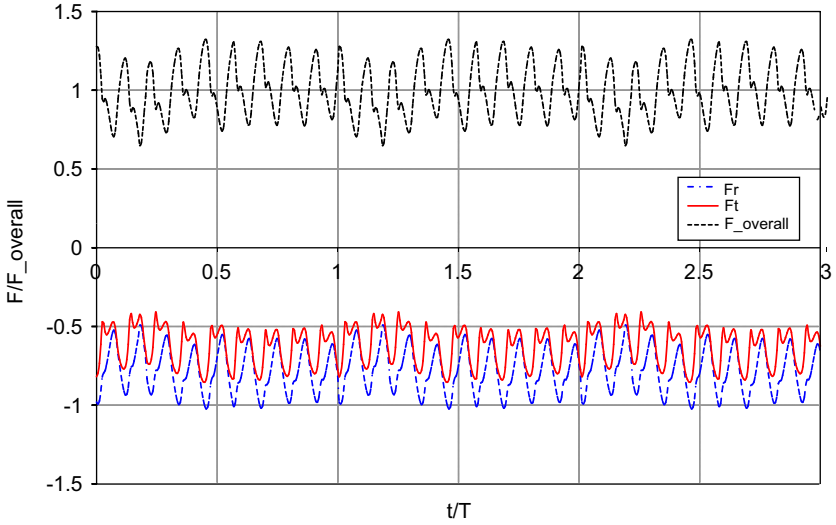

Fig. 11. Force fluctuation vs. time of radial, tangential and overall force over a diffuser blade.

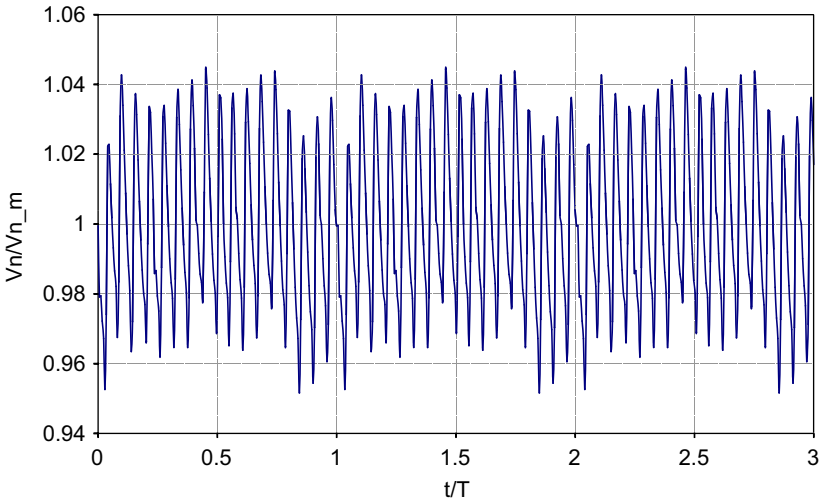

Fig. 12. Normal velocity fluctuation vs. time over an impeller blade.

a numerical modeling with only an impeller. In this case tone noise is due to the mean force on the rotating blades. Thus, it is the interaction between impeller and diffuser blades which is the main cause of the predicted tonal noise.

The acoustic wave length, corresponding to the BPF of the centrifugal fan, is $\lambda = 66\,\text{mm}$. This value is smaller than the impeller blade chord (71.7 mm) and not far exceeding the diffuser blade chord (59.9 mm), so, according to condition (16) the impeller and diffuser blades are not compact. For this reason the impeller and the diffuser blades are divided into parts which ensure the compactness of the sources. Thereby the characteristic length L chosen for the elementary parts is 1.5 mm.

For each compact element of surface blades, the sound pressure generated by the impeller and the diffuser is given by Eqs. (17)–(19) presented in Section 2.

The overall sound pressure for each harmonic (m) is calculated by the following equation:

$$p'^{(m)} = p'^{(m)}_{\text{load1}} + p'^{(m)}_{\text{load2}} + p'^{(m)}_{\text{thickness}}. \tag{20}$$

The sound pressure level is given by

$$L_p = 20\log_{10}\left(\frac{p'^{(m)}}{p_0}\right), \tag{21}$$

$p_0 = 2 \times 10^{-5}$ Pa

Eq. (20) (sum of Eqs. (17)–(19) for each compact element) gives the discrete tonal noise, the broadband noise is not determined by this modeling.

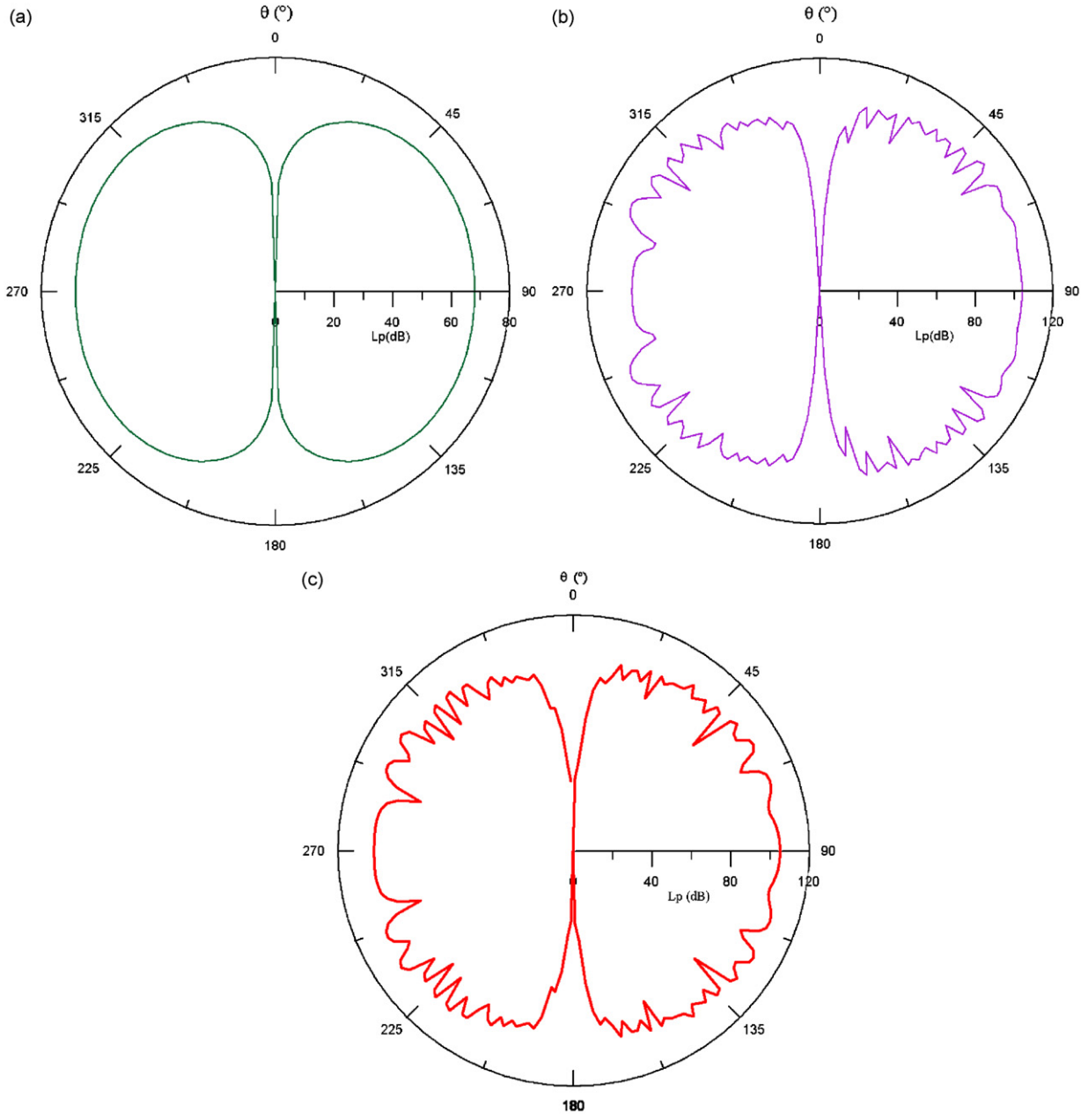

Fig. 13. Numerical dipole noise directivity — $m = 1$, $r_o = 1$ m, $\varphi = \pi/4$: (a) impeller dipole, (b) diffuser dipole, (c) overall dipole.

Figs. 13–15 show the directivity of the first harmonic ($m = 1$) of the dipole, the monopole and the overall sound pressure level respectively, at $r_o = 1$ m. The overall sound pressure level is compared to experimental data.

Fig. 13 presents the impeller, the diffuser and the overall first harmonic dipoles obtained by numerical simulation at $\varphi = \pi/4$ and $r_o = 1$ m. The effect of the diffuser dipole is dominant on the overall dipole. The figure shows that the overall dipole is not symmetric. This is due to the geometry asymmetry of the centrifugal fan. The overall shape of the directivity is function of φ.

The directivity of the thickness sound level is shown in Fig. 14 at $\varphi = \pi/4$ and $r_o = 1$ m. As expected the monopole source is far from being negligible. Its value, quite constant (around 80 dB), is smaller than the dipole sound level, except for the values ranging between $0^\circ \pm 10^\circ$ and $180^\circ \pm 10^\circ$ where the dipole sound level is the lowest with 0 dB at 0° and 180°.

Fig. 15 shows the predicted overall sound level compared to measurements. The difference between the overall sound level and measurements is presented in Fig. 16. As shown in this figure, the difference between measurements and calculation is about 10 dB (over a maximum value of 110 dB) at the radial direction around 90° and 270°, the calculation predict more noise at this direction than measurements. In addition to the assumptions stated above, the reason is that in the theoretical model all the surfaces are considered as acoustically transparent, the effect of the acoustic attenuation of the diffuser blades in the radial direction is not taken into account. In the axial direction, the difference do not exceed 5 dB by taking into account the attenuation of the casing. In this direction the fan radiates in free field.

4.2.1. *Discussion about the overall shape of the directivity*

Fig. 13 shows that the dipole radiated by the diffuser is predominant. By comparing the dipole of Fig. 13 and the monopole in Fig. 14, one can observe that the effect of monopole is important only around the rotational axis (0° and 180°).

Another experimental measurement presented by Fig. 17 shows the acoustic pressure according to the centrifugal fan velocity. One can show that $p' \propto N^2$ for a monopole source by using the dimensional analysis, this mean that the sound power varies in N^4. The acoustic pressure varies in $N^{2.17}$ as given by the fit curve corresponding to measurements. At first sight, the analysis of this result could insinuate that the noise has

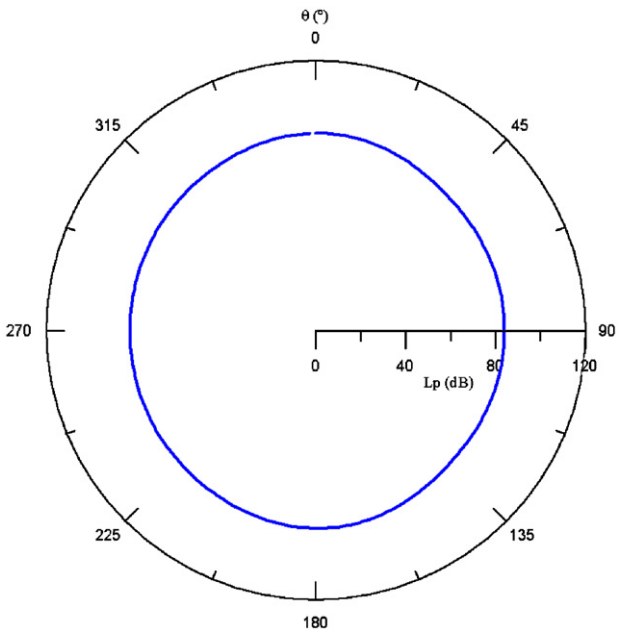

Fig. 14. Numerical monopole noise directivity — $m = 1$, $r_o = 1$ m, $\varphi = \pi/4$.

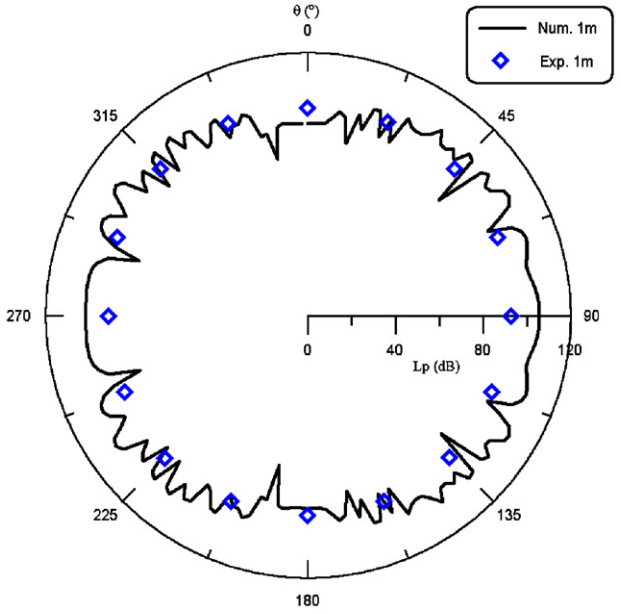

Fig. 15. Numerical and experimental overall noise directivity—$m = 1$, $r_o = 1\,\mathrm{m}$, $\varphi = \pi/4$.

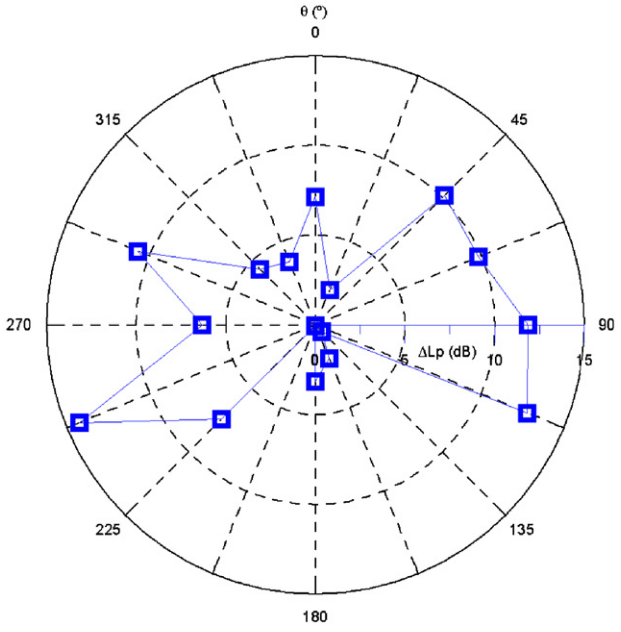

Fig. 16. Difference between directivities obtained by the measurements and the calculations ($\Delta L_p = |L_{p_{\mathrm{exp}}} - L_{p_{\mathrm{num}}}|$) at $m = 1$, $r_o = 1\,\mathrm{m}$ and $\varphi = \pi/4$.

a monopolar nature. But Ffowcs Williams et al. [23] show that sound power of rotational dipoles vary in N^5 for non-compact sources. In other words, the acoustic pressure varies approximatively in $N^{2.5}$. This will lead to the conclusion that the radiation is of dipole type with a non-negligible monopole effect around $\theta = 0^\circ$ and 180°.

An azimuthal asymmetry of directivity in θ direction is observed in Figs. 13 to 17. Fig. 18 shows with some details the 3D behavior of the overall directivity. This representation allows to observe some phenomena

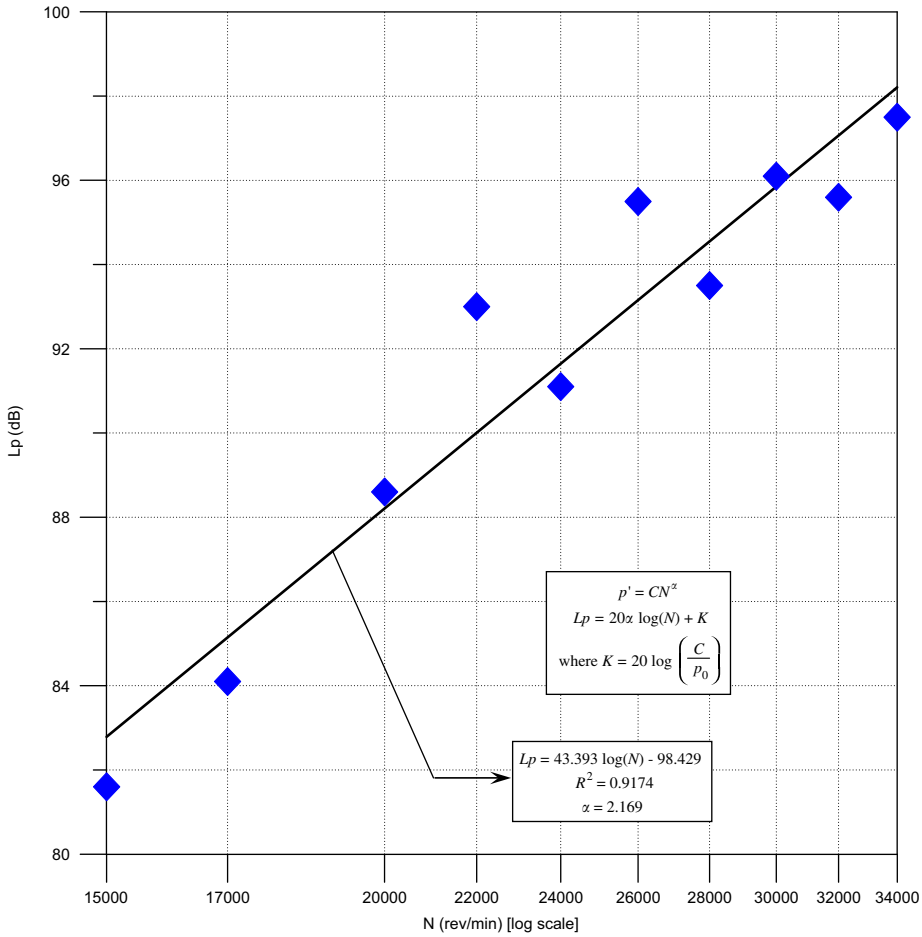

Fig. 17. Acoustic pressure according to rotating velocity.

hidden from view on a 2D representation with a fixed φ angle. In fact, varying the observer position according to angles θ and φ at a constant distance $r_o = 1$ m, Fig. 19 shows the presence of streaks at the directivity sphere circumference for all $\theta \in [45°, 135°]$. It is observed also at the directivity sphere poles (X–Y plane) the presence of a 9-point-star-shaped form. The intermediate zone between star-shaped form and the streaks presents a scattering of the harmonic.

In order to better analyze the topology of the 3D overall directivity, the acoustic level is presented in the $\theta - \varphi$ plane. Fig. 19 shows that the number of streaks is 17 with a variation of $\Delta\varphi = 2\pi/17$ between two consecutive slices, which corresponds to the 17 diffuser blades. The acoustic level on streaks is lower than the one between two successive streaks, this is probably due to the soundproofing effect played by the diffuser blades. At the rotational axis zone (θ near 0 and π), where the effect of the dipole is lower, the figure shows the presence of 9 peaks with a variation of $\Delta\varphi = 2\pi/9$ between two consecutive slices, which corresponds to the 9 blades of the impeller. However, the scattering of the harmonic, observed in Fig. 18, can be explained by the interference between impeller and diffuser blades effects.

5. Conclusion

This work is part of a project whose main objective is the aeroacoustic optimization of high-rotational speed centrifugal fans. We present in this paper the first results which will be used thereafter as an input data to optimum aeroacoustic performances modeling of high-rotational speed vaned centrifugal fans.

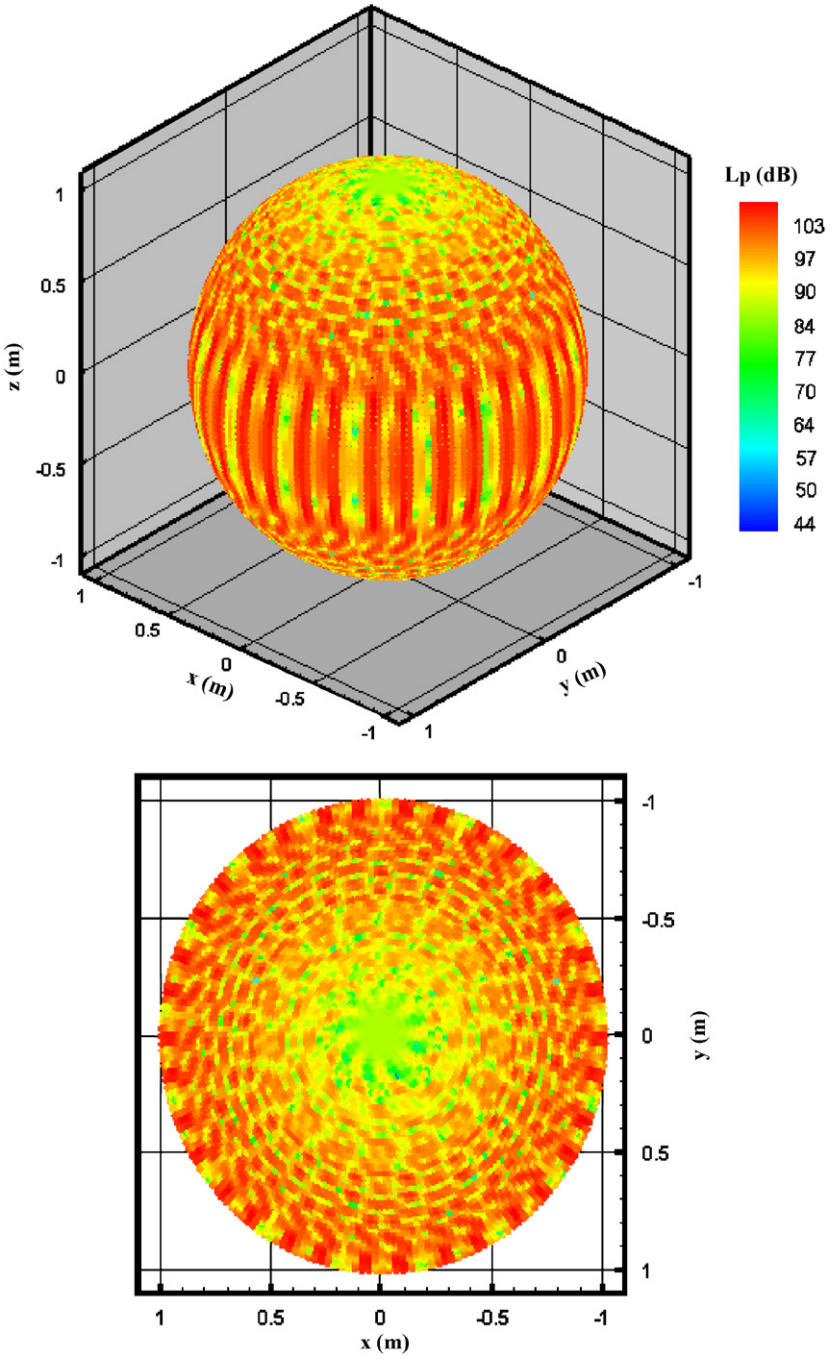

Fig. 18. 3D overall directivity — $m = 1$, $r_o = 1$ m.

As a first stage, a numerical simulation of the aerodynamics of the centrifugal fan is performed. Pressure fluctuation at the impeller–diffuser interface is compared to measurements. The fluctuating pressure is correctly predicted by the numerical simulation. The result shows the importance of the interaction between the impeller and the diffuser. This interaction is at the origin of the tonal noise radiated by the centrifugal fan. The numerical simulation of fluid flow gives also the force and the velocity fluctuation on the impeller and diffuser blades. These two parameters are used as input data for the calculation of the far-field acoustic

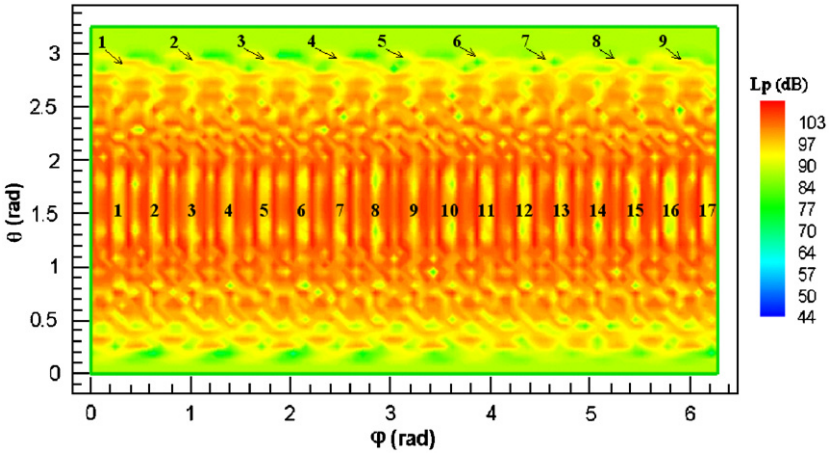

Fig. 19. Overall acoustic pressure level in $\theta - \varphi$ plane—$m = 1$, $r_o = 1$ m.

pressure using the FW&H's equation. Only dipole and monopole sources are calculated. The solution in frequency domain enables to obtain the tonal noise. The result shows that the radiation is of dipole type with a non-negligible monopole effect in the axial directions (around 0° and 180°).

This study, thanks to which our numerical modeling has been validated, will be used in a future work in order to design improved prototypes. The design method will be based on the obtained results of aerodynamics and aeroacoustics. However, the geometry of the impeller and diffuser at the interface will be improved to reduce the pressure gradient in order to decrease the dipole noise source. The impeller will be designed so as to reduce its rotational velocity and therefore the monopole noise source.

References

[1] H. Krain, Review of centrifugal compressor's application and development, *Journal of Turbomachinery* 127 (2005) 25–34.
[2] K. Kim, S. Seo, Shape optimisation of forward-curved-blade centrifugal fan with Navier–Stokes analysis, *Journal of Fluid Engineering* 126 (2004) 735–742.
[3] M. Zangeneh, M. Schleer, Investigation of an inversely designed centrifugal compressor stage–part i: design and numerical verification, *Journal of Turbomachinery* 126 (2004) 73–81.
[4] M. Schleer, S. Hong, Investigation of an inversely designed centrifugal compressor stage–part ii: experimental investigation, *Journal of Turbomachinery* 126 (2004) 82–90.
[5] S. Khelladi, S. Kouidri, F. Bakir, R. Rey, Flow study in the impeller–diffuser interface of a vaned centrifugal fan, *Journal of Fluid Engineering* 127 (2005) 495–502.
[6] S. Seo, K. Kim, S. Kang, Calculations of three-dimentional viscous flow in a multiblade centrifugal fan by modeling blade forces, *Journal of Power and Energy* 217 (2003) 287–297.
[7] W. Neise, Noise reduction in centrifugal fans: a literature survey, *Journal of Sound and Vibration* 45 (1976) 375–403.
[8] W. Neise, G.H. Koopmann, Reduction of centrifugal fan noise by use of resonators, *Journal of Sound and Vibration* 73 (1980) 297–308.
[9] W. Neise, Review of noise reduction methods for centrifugal fans, *Journal of Engineering for Industry* 104 (1982) 151–161.
[10] Parrondo-Gayo, Gonzalez-Perez, Fernandez-Francos, The effect of the operating point on the pressure fluctuations at the blade passage frequency in the volute of a centrifugal pump, *Journal of Fluids Engineering* 124 (2002) 784–790.
[11] W. Jeon, S. Baek, C. Kim, Analysis of the aeroacoustic characteristics of the centrifugal fan in a vacuum cleaner, *Journal of Sound and Vibration* 268 (2003) 1025–1035.
[12] A. Maaloum, S. Kouidri, R. Rey, Aeroacoustic performances evaluation of axial fans based on the unsteady pressure field on the blades surface, *Applied Acoustics* 65 (2004) 367–384.
[13] S. Khelladi, S. Kouidri, F. Bakir, R. Rey, Unsteady flow in multistage centrifugal fans, ASME Heat Transfer/Fluids Engineering Summer Conference, Charlotte, North Carolina, HT-FED2004-56792.
[14] J. Ffowcs Williams, D. Hawkings, Sound generation by turbulence and surfaces in arbitrary motion, *Philosophical Transactions for the Royal Society of London A* 264 (1969) 321–342.
[15] M. Goldstein, Aeroacoustics, McGraw-Hill, New York.

[16] M.J. Lighthill, On sound generated aerodynamically,i general theory, *Proceedings of the Royal Society of London A* 211 (1952) 564–587.
[17] M.J. Lighthill, On sound generated aerodynamically, ii. turbulence as a source of sound, *Proceedings of the Royal Society of London A* 222 (1954) 1–32.
[18] N. Curle, The influence of solid boundaries upon aerodynamic sound, *Proceedings of the Royal Society of London A* 231 (1955) 505–514.
[19] M. Lowson, J. Ollerhead, A theoretical study of helicopter rotor noise, *Journal of Sound and Vibration* 69 (1969) 197–222.
[20] FLUENT, Copyright 2005 Fluent Inc.
[21] F. Menter, Zonal two equation $k-\omega$ turbulence models for aerodynamic flows, AIAA Paper 93-2906.
[22] J. Ferziger, M. Peric, *Computational Methods for Fluid Dynamics*, third ed., Springer, Berlin.
[23] J.E. Ffowcs Willams, L.H. Hall, Aerodynamic sound generation by turbulent flow in the vicinity of a scattering half-plane, *Journal of Fluid Mechanics* 40 (1970) 657–670.